Core(Fe)–Shell(Au) Nanoparticles Obtained from Thin Fe/Au Bilayers Employing Surface Segregation

Dor Amram*,† and Eugen Rabkin†,‡

†Department of Materials Science and Engineering, Technion-Israel Institute of Technology, Haifa 32000, Israel and ‡Institute for Applied Materials, Karlsruhe Institute of Technology, P.O. Box 3640, 76021 Karlsruhe, Germany

ABSTRACT Core(Fe)–shell(Au) nanoparticles are obtained by solid-state dewetting of thin Fe/Au bilayer films deposited on a sapphire substrate. The core–shell morphology is achieved by employing the equilibrium segregation phenomenon, where Au atoms form a homogeneous thin shell on the surfaces of an Fe nanoparticle and at its interface with the substrate, reducing the total interfacial energy of the system. The obtained nanoparticles are single crystalline (structurally perfect), thermally stable, and of high purity. Their size may be tuned by changing the initial film thickness. We demonstrate that the nanoparticles can subsequently be stripped from the substrate, and/or be modified by attaching thiol-containing organic molecules for use in various nanotechnology-related applications. The method presented herein may easily be extended to other metal combinations, especially those relevant for catalysis, thus helping to reduce precious-metal (*e.g.*, Au, Pt, Rh) content in the catalyst.

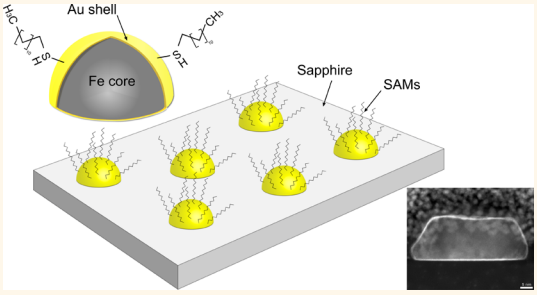

KEYWORDS: nanoparticles · core–shell · segregation · SAMs · Fe/Au

Metal nanoparticles (NPs) and nanostructures are on the forefront of various nanotechnology applications such as sensing devices,[1,2] lubricants,[3] catalysts,[4,5] and strengthening agents in multiphase and composite materials.[6] It is well established that the physical properties of NPs of elemental metals may differ considerably from the bulk properties of the same materials.[7] In many engineering applications in which a material should simultaneously perform several very different functions, NPs containing two (or more) phases have to be used. The chemical identity of the second phase, its relative quantity, and morphological distribution can be tuned to optimize performance.

An interesting example is Fe/Au NPs with a core–shell morphology. Such particles could find promising applications in the data storage,[8] magneto-optical,[9,10] sensing,[11–13] and biomedical fields.[14] A combination of ferromagnetic properties (Fe core) and inertness to a wide range of external conditions (Au shell) is particularly useful. While there have been several reported attempts at producing such NPs, the synthesis methods were usually chemical/electrochemical and therefore led to a fully or partially oxidized Fe core (rather than metallic Fe),[11,14–16] which is known to have a lower saturation magnetization.[17] Such synthesis routes also result in a relatively large concentration of impurities, due to the many solutions and reagents involved, as well as structural defects (such as twin boundaries, grain boundaries, dislocations, *etc.*). In contrast, solid-state dewetting of thin metallic films on a ceramic substrate has been shown to yield defect-free single crystal NPs with a purity which is determined only by the source materials used for deposition of the initial films.[18,19] The NPs may also be arranged periodically on a substrate by means of either film or substrate prepatterning.[20,21] Although several works involving dewetting of thin films made of two components (in the form of either an alloy or a bilayer) can be found in the literature,[21–23] to the best of our knowledge the "tunable" morphology and functional properties of the resulting NPs had not been explored.

One way of obtaining a core(Fe)–shell(Au) NP morphology is by precipitation of Fe

* Address correspondence to doramram@tx.technion.ac.il.

Received for review August 1, 2014 and accepted September 11, 2014.

Published online September 11, 2014
10.1021/nn504284d

inside a particle of a supersaturated Au(Fe) solution, where the driving force for Fe precipitation as a "core" is its large surface energy compared with that of Au.[24,25] This has been attempted in a previous work employing Au-rich compositions.[26] In practice, however, precipitation of the Fe-rich phase occurred at the side facets of the parent Au-rich particle. This was explained by the presence of a thin (~1 nm) Au-rich segregation layer on all surfaces of the Fe precipitate and at its interface with the sapphire substrate. By considering a modified surface energy of Fe (taken to be closer to that of pure Au), a static equilibrium calculation revealed that precipitation is favored inside the parent particle when the precipitate is small, while above a certain critical size the precipitate migrates to the side surface of the parent particle.[26]

The phenomenon of surface and interface segregation in binary alloys is known in physical metallurgy and surface science for over a century.[27] In thermodynamic equilibrium, the drive of the system to reduce its surface energy leads to a difference in surface and bulk compositions of the alloy. The thickness of the segregation layer (usually, about 1 nm) and its composition are uniquely determined by the average alloy composition and temperature. Despite that a spatial extension of the segregation zone is suitable for the microstructural design of NPs, reports in the literature on utilization of equilibrium surface segregation in NPs synthesis are scarce, and the proofs that the surface segregation layer is in a state of thermodynamic equilibrium are missing.[28,29]

RESULTS AND DISCUSSION

In this work we report on the synthesis of core(Fe)–shell(Au) NPs by solid-state dewetting of thin Fe/Au bilayers on a sapphire substrate, taking advantage of the phenomenon of Au segregation on the surface of Fe–Au alloys, to form the Au shell on the Fe NP. An Fe-rich composition was selected to minimize the total volume fraction of Au in the system (so as to minimize the amount of biparticles) while still allowing for full coverage of the Fe NPs by a Au shell. The rest of the experimental conditions (annealing temperature, time, and ambient) were then selected to obtain Fe NPs "encapsulated" by a Au segregation layer. The microstructure of the as-deposited films and their dewetting behavior have already been determined.[30,31] We also demonstrate the ability to bind organic molecules to the NPs, as well as to remove them from the substrate for use in solution.

Figure 1a,b and Figure 1c,d show high-resolution scanning electron microscopy (HRSEM) micrographs of Fe/Au NPs obtained from bilayers of 4 and 30 nm in total thickness, respectively. The relative film thickness corresponds to an Fe composition of ~80 at. % in both cases. The average particle sizes are ~30 nm (for the 4 nm bilayer, labeled "H_S") and ~270 nm (for the 30 nm bilayer, labeled "H_L"), and the ratio

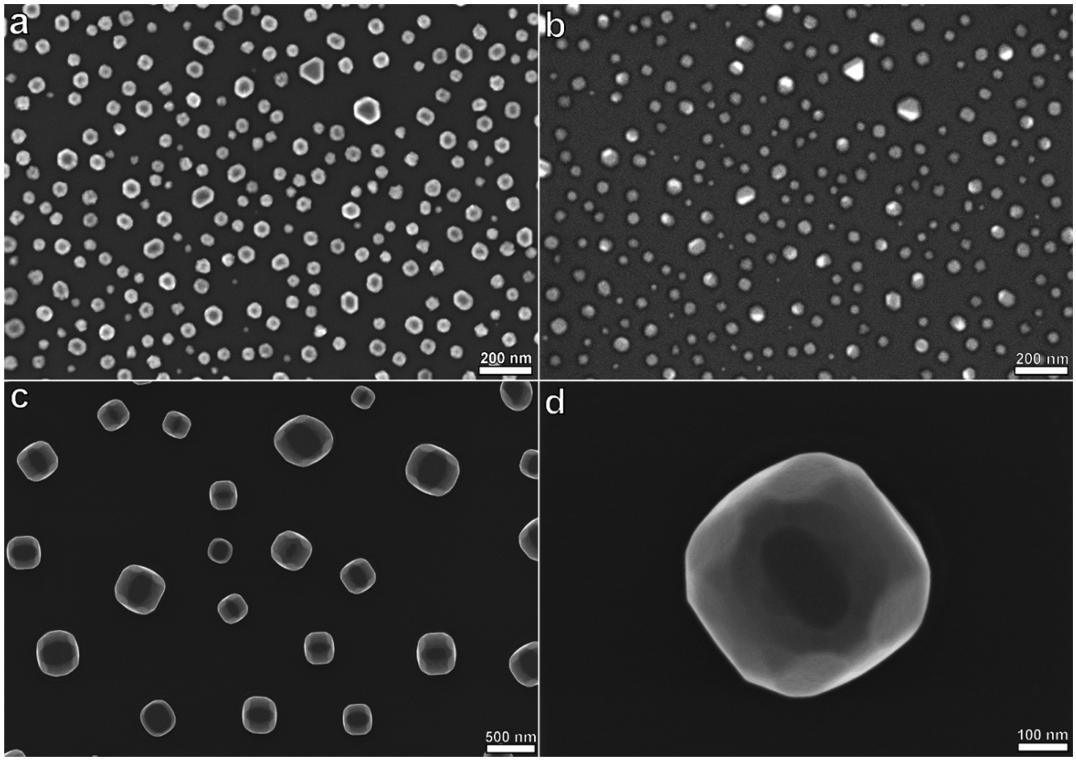

Figure 1. HRSEM micrograph of Fe NPs with a thin Au shell, obtained by annealing Fe/Au bilayers at 1100 °C for 1 h: (a) SE micrograph of particles obtained from a 4 nm thick bilayer; (b) BSE micrograph of the same particles; (c,d) SE micrographs of particles obtained from a 30 nm thick bilayer.

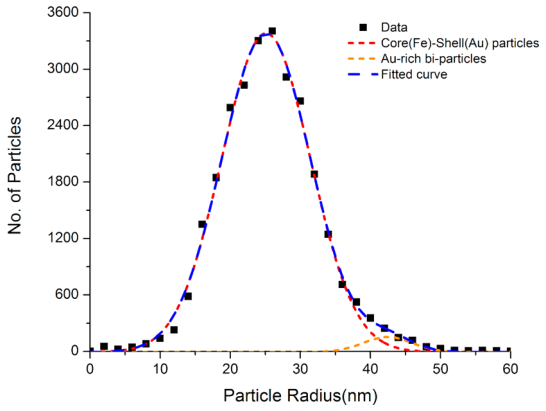

Figure 2. Size distribution of the particles labeled H_S. The data were fitted with a linear combination of two Gaussian functions, representing the core–shell particles (dashed red line) and the Au-rich biparticles (dashed orange line). The sum of the two contributions is represented by the dashed blue line.

between them corresponds approximately to the initial thickness ratio. This is expected since the particles are nearly equiaxed, and it is well-known that the average particle height increases with increasing film thickness.[18] The size distribution of the H_S NPs (Figure 1a,b) is bimodal, in which the population having a larger size are biparticles containing two adjacent alloy phases—Fe(Au) and Au(Fe)—as indicated by the bright contrast in the backscattered electron (BSE) micrograph (Figure 1b). This observation is complemented by the size distribution in Figure 2, which was obtained by image analysis of about 30 000 particles. The radius of each particle was obtained from its projected area assuming a circular shape, and the data were fitted by a linear combination of two Gaussian functions. The large peak corresponds to the core–shell nanoparticles (25 ± 12 nm), while the small peak corresponds to the larger, Au-rich biparticles (42 ± 7 nm). The formation of these biparticles is a kinetic phenomenon, arising from both the incomplete dissolution of a Au-rich phase and local variation of Au concentration during dewetting.[26] The intermixing of Au and Fe in the bilayer is incomplete since the composition and annealing temperature employed in this work correspond to a two-phase area of the bulk Au–Fe phase diagram.[32] This results in local composition gradients already at the beginning of the annealing (*i.e.* when the thin film is in its initial stages of agglomeration), and the subsequent formation of homogeneously dispersed Au-rich particles. To minimize the amount of such particles, the total Au concentration in the bilayer should be further decreased. This concentration is related to the Au/Fe thickness ratio. It should be noted, however, that the average particle size scales with the total film thickness, and keeping both the Au/Fe thickness ratio and the total film thickness small may result in a discontinuous Au film.[30,33] This discontinuity would result in lateral composition variations in the fully agglomerated (dewetted) state. Moreover, even in the case of a full initial intermixing of the layers, lateral variations in concentration occur as a result of a difference in mobility between Au (fast) and Fe (slow) atoms. This would also lead to a lateral kinetic phase separation during dewetting.[34] Nonetheless, the majority of NPs obtained in this work are core–shell nanoparticles which are quite uniform in size. The single crystal, highly faceted nature of the NPs is more clearly observed in the case of the larger H_L NPs (Figure 1c,d).

To characterize the core–shell morphology, cross-sectional transmission electron microscopy (TEM) samples were prepared from both H_S and H_L NPs. Figure 3a shows a high-resolution TEM (HRTEM) cross-section micrograph of a representative H_S NP. The Fe core is a single crystal (does not contain any grain boundaries or other visible defects) and is uniformly covered by a thin layer in dark contrast, which is the Au-rich segregation layer. This has been confirmed in previous experiments[26] by energy-dispersive X-ray spectroscopy (EDXS) in TEM. The Pt, which was deposited in the focused ion beam microscope (FIB) during sample preparation, appears not only on top, but also "through" the NP. This occurs because the NP is thinner than the actual FIB lamella thickness. Further thinning risks the disappearance of the NP since it is not necessarily positioned at the exact center of the lamella's thickness dimension. In Figure 3b, a high-angle annular dark field scanning TEM (HAADF STEM) micrograph of the same NP is shown, and the Au segregation shell (now in white contrast) is clearly visible. Figure 3c is a high-resolution STEM magnification of the area in Figure 3b marked by a dashed rectangle. The Fe/sapphire interface (with the Au-rich segregation layer in between) is clearly observed with atomic resolution. Figure 3d shows a cross section of the particle shown in Figure 1d, which also exhibits Au segregation to all of its surfaces and to its interface with the substrate. Therefore, the size of these NPs can be controlled while maintaining the Au segregation shell.

The thermodynamic driving force for solute segregation to a surface/interface is the reduction in that surface's/interface's energy. Quantitative analysis of the thickness and composition of Au segregation was carried out for the (110) and (100) surfaces of the Fe NPs, the (110)Fe-(0001)sapphire interface and an Fe–Fe low-angle grain boundary. These results, supported by first-principles density functional theory calculations, are beyond the scope of this work and will be published elsewhere.[35] Here, we will show that the selected annealing conditions allow formation of an equilibrium surface segregation layer of Au on single crystalline Fe NPs. Hofmann and Erlewein derived an approximate relationship for the time, t_{sat}, needed to achieve the equilibrium surface concentration in a system with a strong segregation tendency:[36]

$$t_{sat} = \frac{\pi}{4}\frac{s^2\delta^2}{D} \quad (1)$$

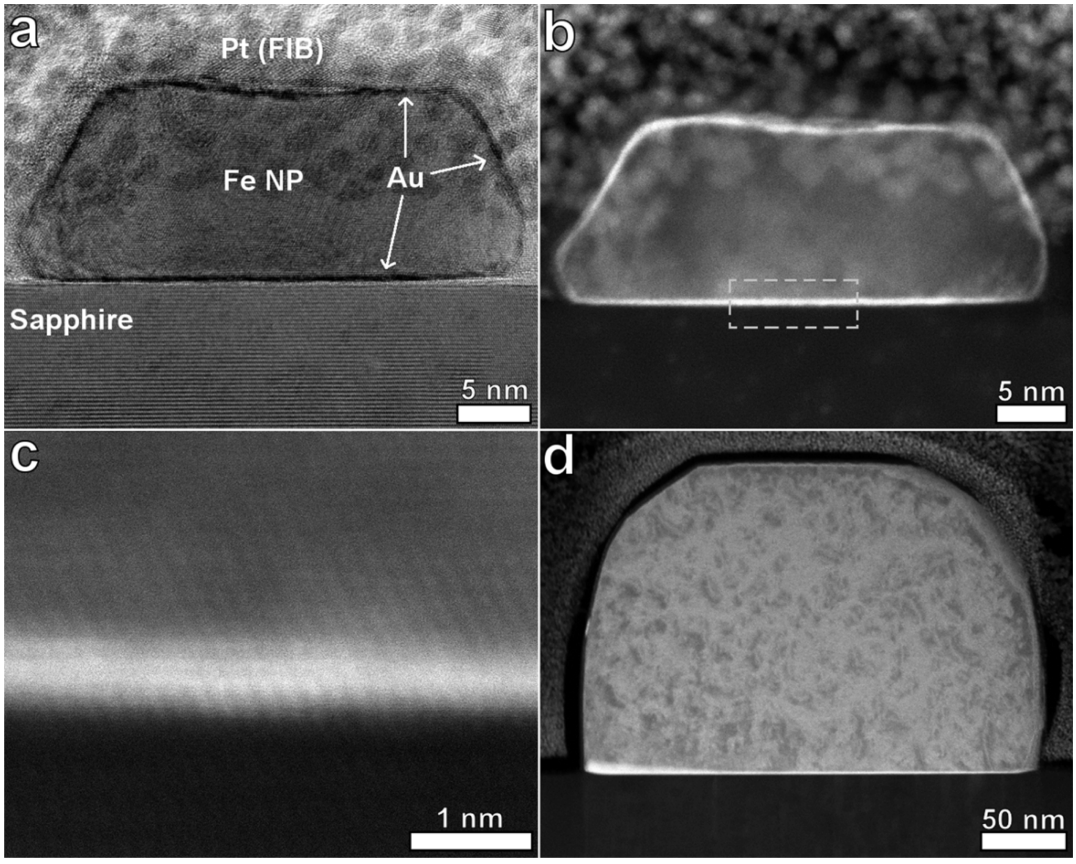

Figure 3. Cross-sectional TEM of Fe NPs with a thin Au shell. (a) HRTEM micrograph of one of the Fe NPs shown in Figure 1a. The Au segregation layer surrounding the Fe particle is seen in dark contrast. (b) HAADF STEM micrographs of the same NP as in panel a. The Au segregation layer surrounding the Fe particle is seen in white contrast. (c) High-resolution magnification of the dashed rectangle in panel b, showing Au segregation to the sapphire/Fe interface. (d) STEM micrograph of the Fe NP shown in Figure 1d.

where s, δ, and D are the surface enrichment factor, the width of the surface segregation layer, and the bulk heterodiffusion coefficient of the segregating species in the crystal, respectively. The values of s and δ determined in our companion study[35] are 4.1 and 0.72 nm, respectively. The heterodiffusion coefficient of Au in paramagnetic α-Fe was determined by Borg and Lai,[36] and extrapolating their data to the temperature employed in this study (1100 °C) yields $D = 3.6 \times 10^{-13}$ m^2 s^{-1}. With these data, eq 1 yields $t_{sat} \approx 20$ μs, which is significantly shorter than the annealing time of 1 h employed in this study. Thus, the selected annealing conditions indeed ensure the formation of an equilibrium Au-rich surface segregation layer on the Fe/Au NPs. In our estimates we employed the heterodiffusion coefficient of Au in α-Fe, rather than in γ-Fe, despite the fact that the latter is the stable allotrope at the temperature of 1100 °C. This is because the $\alpha \rightarrow \gamma$ phase transformation was not observed in our *in situ* X-ray diffraction experiments performed on the thin bilayer films employed in this study. The crystal structure of the Fe at room temperature thus remained body centered cubic (bcc).

It is important to emphasize that both the Fe core and Au shell of the NPs are alloys rather than pure materials. The solubility of Au in Fe is about 1 at. % at 850 °C and decreases with decreasing temperature; Au content at this low level has a negligible effect on the magnetic properties of Fe,[32] though it could improve its resistance to oxidation.[26] On the other hand, the solubility of Fe in Au is large and, therefore, the Au-rich segregation shell contains a significant amount of Fe.[35]

The poor adhesion of the metallic particles to the ceramic substrate allows one to separate them when the contact area is sufficiently small (*i.e.*, small particle diameter). Figure 4 shows TEM micrographs of the H_S NPs removed from the substrate by stripping and placed on a TEM grid. Figure 4a shows that some of the stripped particles are the Au-rich ones observed in Figure 1b. Figure 4b,c shows that the core–shell NPs, and the Au coverage can clearly be observed. The ability to separate the core–shell NPs from the substrate may further be utilized to transfer them into various solvents or other substrates. In this work we demonstrate that organic molecules can be bonded to the NPs, with implications in the biomedical field (*e.g.*, targeted drug delivery). The molecule of choice was 1-dodecanethiol due to the strong covalent

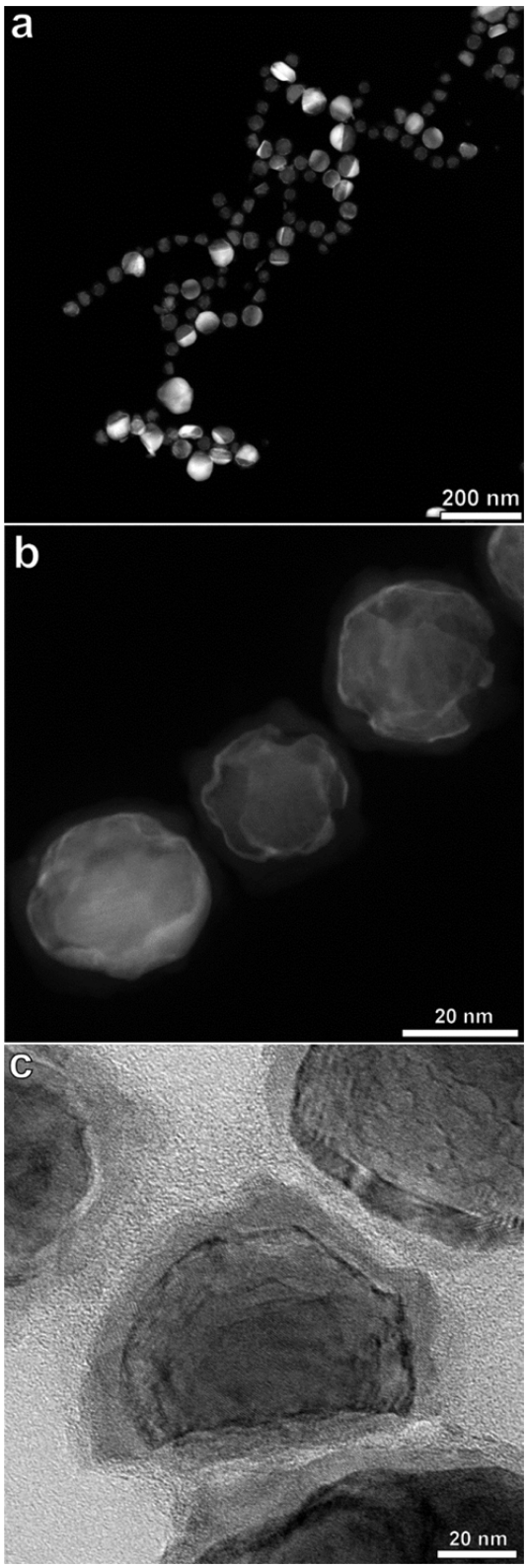

Figure 4. (a,b) HAADF STEM and (c) TEM micrographs of Fe/Au NPs which were stripped from the substrate and placed on a TEM grid.

bond between S and Au, and the tendency to form hydrophobic self-assembled monolayers (SAMs) by parallel alignment of the alkyl chains.[37] Therefore, their presence may be identified in simple wetting (contact angle) experiments. The results are summarized in Table 1.

TABLE 1. Contact Angles for Different NPs and the Bare Substrate, with and without SAMs

		measured contact angle	calculated contact angle
	SAMs[a]	[deg][b]	[deg]
bare sapphire	*X*	65	*c*
	V	64	*c*
Au NPs	*X*	72	72
	V	91	89
Fe NPs	*X*	68	67
	V	60	67
core—shell Fe/Au NPs	*X*	68	68
	V	75	74

[a] *V* and *X* indicate "with SAMs" and "without SAMs", respectively. [b] The typical error of contact angle measurements was 2—4°. [c] The measured values were employed as parameters for the model (θ_s), and therefore their calculation by the model is redundant.

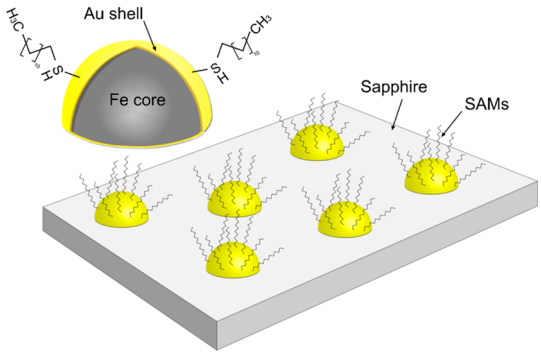

Figure 5. Illustration of the core(Fe)—shell(Au) NP morphology, and the binding of 1-dodecanethiol molecules to the Au surface of the particles, forming SAMs.

The contact angle of water on sapphire is not affected by the application of SAMs, since the latter do not form any bonds with sapphire and are removed by the postimmersion washing. For pure Au NPs, the contact angle increases after application of SAMs, due to the bonding with Au and their hydrophobic nature. In contrast, for pure Fe NPs the contact angle decreases after application of SAMs, despite the fact that no bonding is expected. This can be explained by oxidation or hydroxylation of Fe after or during immersion in the SAMs solution, yielding a lower surface energy. The Fe NPs oxidize very slowly in air due to their single crystalline nature, and even cross-sectional TEM samples showed minimal signs of oxidation from both sides of the lamella.[26] Finally, the core(Fe)—shell(Au) NPs show an expected increase in contact angle, similar to Au NPs. The contact angles obtained in wetting experiments with Fe/Au and Au NPs are different because of the differences in the particle sizes and interparticle distances (*i.e.*, differences in the area fraction of the exposed substrate). Figure 5 illustrates schematically the obtained core(Fe)—shell(Au) NPs

after application of SAMs. The macroscopic nature of the wetting experiment allowed us to probe the surface state of millions of NPs, as opposed to TEM observations which are very local in nature. It should be noted, however, that such wetting measurements provide only an indirect evidence for the surface state of the particles. Therefore, we suggested a simple model based on the Cassie–Bexter approach:[38] Consider a planar substrate covered uniformly by particles. The contact angle of a liquid droplet on this heterogeneous surface, θ, can be expressed as

$$\cos(\theta) = \left(\frac{\gamma_s - \gamma_{sl}}{\gamma_l}\right)(1-f) + kf\left(\frac{\gamma_p - \gamma_{pl}}{\gamma_l}\right) \quad (2)$$

where γ_p, γ_s, γ_l, γ_{pl} and γ_{sl} represent the energies of the particle, substrate, and liquid surfaces, and of the particle–liquid and substrate–liquid interfaces, respectively; f is the area fraction of the particles on the substrate and k is the ratio of the surface area of a particle to its contact area with the substrate. The justification for using such a model is that the drop radius (of the order of 1 mm) is much larger than both the particle diameter (<50 nm) and interparticle distance (<200 nm, according to the coverage f obtained by image analysis). To minimize errors which may arise from using surface and interface energies from different literature sources, a series of wetting experiments on reference samples was performed, such that no external parameters were required, with the exception of f and k. The geometric parameter k was calculated assuming coin-shaped particles of height h and radius r, where typically $h \approx r/4$. In that case, $k = 1.5$ is obtained (for a hemispherical particle $k = 2$).

Thus, for a given sample containing particles, the contact angle was calculated according to eq 2:

$$\cos(\theta) = (1-f)\cos(\theta_s) + kf\cos(\theta_p) \quad (3)$$

where θ_s is the measured contact angle of water on c plane sapphire, and θ_p is the measured contact angle of water on either Au, Fe, or Au covered with SAMs. The former was obtained by measurements on the bare substrate, while the latter by measurements on the thin film samples (Au, Fe, and Au covered with SAMs). The advantage of this method is that it is independent of the actual surface and interface energies in the system, and errors arise solely due to the contact angle analysis and sample preparation techniques, which were identical for all samples. The contact angles for the different NPs calculated with the aid of this model were in good agreement with the experimental results (Table 1).

CONCLUSIONS

We obtained core(Fe)–shell(Au) NPs by solid-state dewetting of thin Fe/Au bilayer films deposited on a sapphire substrate. The NPs are single crystalline and have the purity of the original evaporation targets. Their size may be tuned by changing the initial film thickness. The core–shell morphology was achieved by taking advantage of equilibrium Au segregation to all surfaces and interfaces of the Fe particles, and by selecting the appropriate experimental conditions—composition and annealing time and temperature. These NPs can subsequently be stripped from the substrate, and/or be modified by attaching organic molecules containing a thiol group, for use in various nanotechnology-related applications.

MATERIALS AND METHODS

Electron-beam deposition was employed to deposit Fe and Au layers (5N purity) on c plane oriented sapphire ((0001) singe crystal α-Al_2O_3) substrates. Two total film thicknesses were chosen: 3 nm (Fe) and 1 nm (Au) (4 nm total thickness), and 22 nm (Fe) and 8 nm (Au) (30 nm total thickness). The thickness ratio in both cases corresponds to a composition of ~80 at. % Fe. The polished sapphire wafers were 2″ in diameter and 430 μm in thickness (University Wafers), with a miscut of up to 0.2° toward the m plane. Prior to deposition the sapphire wafers were cleaned in a clean room with soap, acetone, isopropanol and deionized water followed by dipping in Piranha solution (2 H_2SO_4: 1 H_2O_2 by vol.), deionized water, and a low temperature bake at 120 °C. Deposition was performed at room temperature in a vacuum chamber with a base pressure of 3×10^{-7} Torr. The deposition rate was 0.3 Å s^{-1} for both layers. Annealing of the samples was performed in a Rapid Thermal Annealing furnace (RTA; ULVAC-RIKO MILA 5000 P–N) under forming gas flow (Ar-10% H_2, 6N purity), at a temperature of 1100 °C for 1 h. A heating rate of 50 °C s^{-1} was used and fast cooling was performed by simply switching off the heating. To avoid contaminations, samples were placed on a sapphire plate, which in turn was placed on a quartz holder.

The particles were characterized by high-resolution scanning electron microscopy (HRSEM; Zeiss Ultra Plus). HRSEM micrographs were taken using either an in-lens secondary electron (SE) detector or a backscattered electron (BSE) detector, at an acceleration voltage of 2 keV. A thin carbon film (<4 nm) was deposited on the sample prior to SEM analysis in order to prevent charging. High-resolution transmission electron microscopy (HRTEM; FEI Titan 80-300 keV S/TEM) was used to analyze cross-section samples, prepared by the lift-out method in a focused ion beam (FIB; FEI Strata 400-S).[39] The FIB lamellae were positioned on a Ti grid and further thinned by low-kV milling using Ar+ ions at an energy of 500 eV (Linda GentleMill3).

Stripping of the particles from the substrate was performed by depositing a drop of collodion solution on the sample (collodion 2% in amyl acetate; EMS), and letting the solvent evaporate. The resulting collodion film on the surface was then stripped from the substrate using tweezers, and placed on a carbon-coated Cu grid. The grid was then placed on filter paper soaked with amyl acetate, dissolving the collodion film. The stripped nanoparticles adhered to the carbon film on the grid, and were characterized by TEM.

Contact angles were measured with an optical tensiometer (Attension Theta) using deionized water droplets (7 ± 1 μL). For comparison, the following systems were analyzed: Fe NPs; Fe thin film; Au NPs; Au thin film; Fe/Au NPs; Fe/Au thin bilayer; c plane sapphire substrate. The Fe and Au NPs were obtained by annealing the respective films in the RTA furnace described above.

For each system, two samples were analyzed: one sample was immersed in a solution of 1-dodecanethiol (≥98%, Aldrich) in dry ethanol (concentration of 5 mM) for 24 h followed by drying at room temperature; while the other sample was in as-deposited or as-annealed condition. Eight to ten droplets were analyzed for each sample.

Conflict of Interest: The authors declare no competing financial interest.

Acknowledgment. This work was supported by the Russell Berrie Nanotechnology Institute at the Technion. The thin film deposition was done at the micro and nano fabrication unit (MNFU), Technion. The authors wish to thank Mrs. Sasha Pechook and Prof. Boaz Pokroy for their assistance and advice with contact angle measurements.

REFERENCES AND NOTES

1. De, M.; Ghosh, P. S.; Rotello, V. M. Applications of Nanoparticles in Biology. *Adv. Mater.* **2008**, *20*, 4225–4241.
2. Peng, G.; Tisch, U.; Adams, O.; Hakim, M.; Shehada, N.; Broza, Y. Y.; Billan, S.; Abdah-Bortnyak, R.; Kuten, A.; Haick, H. Diagnosing Lung Cancer in Exhaled Breath Using Gold Nanoparticles. *Nat. Nanotechnol.* **2009**, *4*, 669–673.
3. Zhao, Y.; Zhang, Z.; Dang, H. Fabrication and Tribological Properties of Pb Nanoparticles. *J. Nanoparticle Res.* **2004**, *6*, 47–51.
4. Park, J.; Kang, E.; Son, S. U.; Park, H. M.; Lee, M. K.; Kim, J.; Kim, K. W.; Noh, H.-J.; Park, J.-H.; Bae, C. J.; *et al.* Monodisperse Nanoparticles of Ni and NiO: Synthesis, Characterization, Self-Assembled Superlattices, and Catalytic Applications in the Suzuki Coupling Reaction. *Adv. Mater.* **2005**, *17*, 429–434.
5. Park, J. Y.; Zhang, Y.; Grass, M.; Zhang, T.; Somorjai, G. A. Tuning of Catalytic CO Oxidation by Changing Composition of Rh–Pt Bimetallic Nanoparticles. *Nano Lett.* **2008**, *8*, 673–677.
6. Breval, E.; Dodds, G.; Pantano, C. G. Properties and Microstructure of Ni–Alumina Composite Materials Prepared by the Sol/Gel Method. *Mater. Res. Bull.* **1985**, *20*, 1191–1205.
7. Handwerker, C. A.; Pollock, T. M. Emerging Science and Research Opportunities for Metals and Metallic Nanostructures. *JOM* **2014**, *66*, 1321–1341.
8. Bian, B.; Hirotsu, Y.; Sato, K. Structures and Magnetic Properties of Oriented Fe/Au and Fe/Pt Nanoparticles on a-Al_2O_3. *J. Electron Microsc. (Tokyo)* **1999**, *48*, 753–759.
9. Liu, H. L.; Wu, J. H.; Min, J. H.; Kim, Y. K. Synthesis of Monosized Magnetic-Optical AuFe Alloy Nanoparticles. *J. Appl. Phys.* **2008**, *103*, 07D529.
10. Chiang, I.-C.; Chen, D.-H. Synthesis of Monodisperse FeAu Nanoparticles with Tunable Magnetic and Optical Properties. *Adv. Funct. Mater.* **2007**, *17*, 1311–1316.
11. Liu, T.-S.; Kang, T.-F.; Lu, L.-P.; Zhang, Y.; Cheng, S.-Y. Au–Fe(III) Nanoparticle Modified Glassy Carbon Electrode for Electrochemical Nitrite Sensor. *J. Electroanal. Chem.* **2009**, *632*, 197–200.
12. Le, F.; Brandl, D. W.; Urzhumov, Y. A.; Wang, H.; Kundu, J.; Halas, N. J.; Aizpurua, J.; Nordlander, P. Metallic Nanoparticle Arrays: A Common Substrate for Both Surface-Enhanced Raman Scattering and Surface-Enhanced Infrared Absorption. *ACS Nano* **2008**, *2*, 707–718.
13. Kuznetsov, A. I.; Evlyukhin, A. B.; Gonçalves, M. R.; Reinhardt, C.; Koroleva, A.; Arnedillo, M. L.; Kiyan, R.; Marti, O.; Chichkov, B. N. Laser Fabrication of Large-Scale Nanoparticle Arrays for Sensing Applications. *ACS Nano* **2011**, *5*, 4843–4849.
14. Hien Pham, T. T.; Cao, C.; Sim, S. J. Application of Citrate-Stabilized Gold-Coated Ferric Oxide Composite Nanoparticles for Biological Separations. *J. Magn. Magn. Mater.* **2008**, *320*, 2049–2055.
15. Lyon, J. L.; Fleming, D. A.; Stone, M. B.; Schiffer, P.; Williams, M. E. Synthesis of Fe Oxide Core/Au Shell Nanoparticles by Iterative Hydroxylamine Seeding. *Nano Lett.* **2004**, *4*, 719–723.
16. Chen, M.; Yamamuro, S.; Farrell, D.; Majetich, S. a. Gold-Coated Iron Nanoparticles for Biomedical Applications. *J. Appl. Phys.* **2003**, *93*, 7551.
17. Gangopadhyay, S.; Hadjipanayis, G.; Dale, B.; Sorensen, C.; Klabunde, K.; Papaefthymiou, V.; Kostikas, A. Magnetic Properties of Ultrafine Iron Particles. *Phys. Rev. B* **1992**, *45*, 9778–9787.
18. Thompson, C. V. Solid-State Dewetting of Thin Films. *Annu. Rev. Mater. Res.* **2012**, *42*, 399–434.
19. Malyi, O.; Klinger, L.; Srolovitz, D. J.; Rabkin, E. Size and Shape Evolution of Faceted Bicrystal Nanoparticles of Gold on Sapphire. *Acta Mater.* **2011**, *59*, 2872–2881.
20. Wang, D.; Ji, R.; Schaaf, P. Formation of Precise 2D Au Particle Arrays *via* Thermally Induced Dewetting on Pre-Patterned Substrates. *Beilstein J. Nanotechnol.* **2011**, *2*, 318–326.
21. Oh, Y.-J.; Kim, J.-H.; Thompson, C. V.; Ross, C. A. Templated Assembly of Co–Pt Nanoparticles *via* Thermal and Laser-Induced Dewetting of Bilayer Metal Films. *Nanoscale* **2013**, *5*, 401–407.
22. Krishna, H.; Favazza, C.; Sureshkumar, R.; Kalyanaraman, R. Laser-Induced Dewetting Nanomorphologies in Single and Bilayer Metal Films. *MRS Proc.* **2011**, *960*, 0960–N03–02.
23. Wang, D.; Schaaf, P. Ni–Au Bi-Metallic Nanoparticles Formed *via* Dewetting. *Mater. Lett.* **2012**, *70*, 30–33.
24. Sadan, H.; Kaplan, W. D. Au–Sapphire (0001) Solid–Solid Interfacial Energy. *J. Mater. Sci.* **2006**, *41*, 5099–5107.
25. Tyson, W. R.; Miller, W. A. Surface Free Energies of Solid Metals: Estimation from Liquid Surface Tension Measurements. *Surf. Sci.* **1977**, *62*, 267–276.
26. Amram, D.; Klinger, L.; Rabkin, E. Phase Transformations in Au(Fe) Nano- and Microparticles Obtained by Solid State Dewetting of Thin Au–Fe Bilayer Films. *Acta Mater.* **2013**, *61*, 5130–5143.
27. Gibbs, J. W. On the Equilibrium of Heterogeneous Substances. *Am. J. Sci.* **1878**, *16*, 441–458.
28. Wang, D.; Xin, H. L.; Yu, Y.; Wang, H.; Rus, E.; Muller, D. A.; Abruña, H. D.; Abrun, H. D. Pt-Decorated PdCo@Pd/C Core–Shell Nanoparticles with Enhanced Stability and Electrocatalytic Activity for the Oxygen Reduction Reaction. *J. Am. Chem. Soc.* **2010**, *132*, 17664–17666.
29. Barcaro, G.; Fortunelli, A.; Polak, M.; Rubinovich, L. Patchy Multishell Segregation in Pd–Pt Alloy Nanoparticles. *Nano Lett.* **2011**, *11*, 1766–1769.
30. Amram, D.; Rabkin, E. On the Role of Fe in the Growth of Single Crystalline Heteroepitaxial Au Thin Films on Sapphire. *Acta Mater.* **2013**, *61*, 4113–4126.
31. Amram, D.; Klinger, L.; Rabkin, E. Anisotropic Hole Growth during Solid-State Dewetting of Single-Crystal Au–Fe Thin Films. *Acta Mater.* **2012**, *60*, 3047–3056.
32. Okamoto, H.; Massalski, T. B.; Swartzendruber, L. J.; Beck, P. A. The Au–Fe (Gold-Iron) System. *Bull. Alloy Phase Diagrams* **1984**, *5*, 592–601.
33. Markov, I. V. *Crystal Growth for Beginners*, 2nd ed.; World Scientific: Singapore, 2003; pp 433–440.
34. Herz, A.; Wang, D.; Kups, T.; Schaaf, P. Solid-State Dewetting of Au/Ni Bilayers: The Effect of Alloying on Morphology Evolution. *J. Appl. Phys.* **2014**, *116*, 044307.
35. Amram, D.; Amouyal, Y.; Rabkin, E. 2014, unpublished work.
36. Hofmann, S.; Erlewein, J. Determination of the Diffusion Coefficient of Foreign Atoms in Metals *via* Surface Segregation. *Scr. Metall.* **1976**, *10*, 857–860.
37. Poirier, G. E.; Tarlov, M. J. The c(4 × 2) Superlattice of *N*-Alkanethiol Monolayers Self-Assembled on Au(111). *Langmuir* **1994**, *10*, 2853–2856.
38. Bonn, D.; Eggers, J.; Indekeu, J.; Meunier, J.; Rolley, E. Wetting and Spreading. *Rev. Mod. Phys.* **2009**, *81*, 739–805.
39. Giannuzzi, L. A.; Stevie, F. A. A Review of Focused Ion Beam Milling Techniques for TEM Specimen Preparation. *Micron* **1999**, *30*, 197–204.